

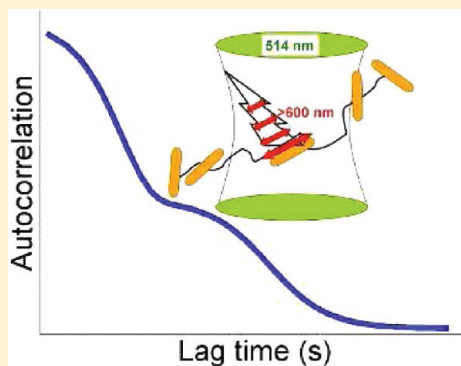
# One-Photon Plasmon Luminescence and Its Application to Correlation Spectroscopy as a Probe for Rotational and Translational Dynamics of Gold Nanorods

Alexei Tcherniak,<sup>†,‡</sup> Sergio Dominguez-Medina,<sup>†,‡</sup> Wei-Shun Chang,<sup>‡</sup> Pattanawit Swanglap,<sup>‡</sup> Liane S. Slaughter,<sup>‡</sup> Christy F. Landes,<sup>\*,‡</sup> and Stephan Link<sup>\*,‡,§</sup>

<sup>†</sup>Department of Chemistry, and <sup>§</sup>Department of Electrical and Computer Engineering, Laboratory for Nanophotonics, Rice University, Houston, Texas 77005, United States

 Supporting Information

**ABSTRACT:** A strong intrinsic signal is advantageous over labeling for optical detection of nanoparticles. Intense scattering and absorption by the surface plasmon resonance, which exceeds molecular cross sections, provides a direct method for visualizing noble metal nanoparticles. While two-photon luminescence in gold nanoparticles yields a strong signal, one-photon luminescence is generally regarded to be much weaker and has seldom been employed for optical nanoparticle detection. In this article we investigated one-photon luminescence of gold nanospheres and nanorods using single particle spectroscopy with excitation at 514 and 633 nm. We characterized the polarization dependence, determined the quantum yield, and present a mechanism describing one-photon luminescence. Our results suggest fast interconversion between surface plasmons and hot electron–hole pairs and show that the luminescence occurs via emission by a surface plasmon. Using the information obtained from the single particle studies, we were able to successfully employ one-photon luminescence for correlation spectroscopy measurements and to correctly interpret auto- and cross-correlation functions, which were used to determine the hydrodynamic sizes of several gold nanoparticle samples and to extract rotational dynamics of nanorods. Because of the difference in size dependence for one-photon luminescence compared to scattering, luminescence correlation spectroscopy of metal nanoparticles is advantageous as it is not as strongly affected by the presence of larger nanoparticles or aggregates. This was verified by measuring luminescence as well as scattering correlation traces for a mixture of nanoparticles containing 98% 57 nm and 2% 96 nm gold nanospheres.



## INTRODUCTION

Any practical application of nanoparticles (NPs) inevitably involves answering questions about NP mobility and aggregation for the various media in which they will be applied. For example, it is important to understand the diffusion of NPs inside cells for their biomedical applications.<sup>1–3</sup> There are two general strategies to optically visualize NPs in solution. One is labeling NPs with fluorescent dyes,<sup>4–8</sup> and the other involves using an intrinsic optical signal, e.g., luminescence, scattering, or absorption.<sup>9–16</sup> For plasmonic NPs, visualization is possible by exploiting their enhanced scattering and absorption cross sections at the surface plasmon resonance.<sup>12–16</sup> Multiphoton luminescence has also been used for noble metal NPs on substrates and in solution.<sup>17–22</sup>

Besides translational diffusion, NPs in solution also undergo rotational diffusion. For nanorods, the rotational diffusion constant,  $D_{\text{rot}}$ , is more sensitive to the length,  $L$ , and aspect ratio, AR, compared to the translational diffusion constant,  $D_{\text{tr}}$ . A number of phenomenological descriptions exist for rotational diffusion, but they all share a common functional form of  $D_{\text{rot}} \sim (1/L^3) \ln(\text{AR})$ , while translational diffusion scales as  $D_{\text{tr}} \sim (1/L) \ln(\text{AR})$ .<sup>23</sup> Because of this steeper length dependence, measuring

the rotational instead of the translational diffusion constant is more sensitive for determining the hydrodynamic radius of nanorods. This fact has been taken advantage of in monitoring nonspecific binding of bovine serum albumin to peptide-coated semiconductor nanorods.<sup>24</sup>

To observe rotational NP diffusion, the measured signal has to be anisotropic and intrinsic to the NP. In case of nanorods, the signal is typically polarized along either or both of the two major axes. For gold nanorods (AuNRs), it has been shown that scattering,<sup>25,26</sup> absorption,<sup>27,28</sup> and two-photon luminescence<sup>17,20</sup> are highly polarized and correlate well with the orientation of the AuNR. Mainly surface plasmon scattering has been utilized to track the rotation of AuNRs in solution as well as attached to glass surfaces, biomembranes, F<sub>1</sub>-ATPase, or microtubules by dark-field imaging and differential interference contrast microscopy.<sup>29–34</sup>

In addition to the optical signal, one can distinguish between two common methods for studying diffusion of plasmonic NPs: One approach is single particle tracking,<sup>35–38</sup> which works best

Received: July 1, 2011

Published: July 12, 2011

for diffusion on surfaces or in thin films because NPs drifting out of focus makes the measurement and analysis difficult or requires complex setups. A second method is to follow not a single NP, but to monitor changes in signal due to NP diffusion from a small focal volume. This approach, pioneered as fluorescence correlation spectroscopy,<sup>39–43</sup> measures the unconstrained three-dimensional diffusion of NPs and offers advantages over bulk measurements because of high spatial resolution—observation volumes are on the order of femtoliters—and the ability to work with low concentrations—nanomolar range. Small detection volumes have the additional benefit of an improved signal to background ratio, because the background signal is reduced for smaller collection areas.

For the correct interpretation of diffusion times obtained from correlation spectroscopy, it is important to consider the size scaling of the particular optical process detected, especially if the system of interest is inhomogeneous containing a distribution of NP sizes. In particular, because the plasmon scattering intensity  $I$  scales as the square of the NP volume ( $I \sim V^2$ ) for NPs smaller than about 100 nm,<sup>44,45</sup> scattering correlation spectroscopy of plasmonic NPs is very sensitive to the presence of larger and hence brighter NPs and NP aggregates, potentially biasing the recovered diffusion constants.<sup>13,14</sup> In contrast, the plasmon absorption intensity  $I$  only scales as the NP volume  $V$  ( $I \sim V$ ) and hence would be preferred for correlation spectroscopy measurements.<sup>44–46</sup> However, absorption-based approaches such as photothermal correlation spectroscopy require careful adjustment of two laser beams.<sup>15,16</sup> Ease of experimental implementation is therefore also an issue that needs to be considered for high throughput screening of NP sizes in solution, making multiphoton luminescence detection less attractive as well because it is only possible with more expensive ultrafast lasers.<sup>21,22</sup>

Ensemble and single particle measurements of gold nanospheres (AuNSs) have shown that, similar to absorption, one-photon luminescence also scales with the NP volume.<sup>46,47</sup> Luminescence correlation spectroscopy of plasmonic NPs requires relatively simple and inexpensive setups, has been well-established for fluorescent molecules, and offers good control over polarization for the measurement of rotational diffusion constants. However, one-photon luminescence of gold NPs is generally a low efficiency process and is therefore not commonly used for NP detection.<sup>46–52</sup> More importantly, the origin of one-photon luminescence remains a subject of debate with proposed mechanisms including plasmon-enhanced interband transitions<sup>48,52–54</sup> or direct plasmon emission.<sup>47</sup> A recent report by Gaiduk et al. also showed that the luminescence of AuNSs in organic solvents can be enhanced under strong laser excitation, which was attributed to temperature-assisted chemical modifications of the NP surface suggesting a surface dependent process.<sup>55</sup>

If it is possible to establish a mechanism for one-photon luminescence of AuNRs and its polarization dependence, luminescence correlation spectroscopy of AuNRs has the advantages of being more sensitive by measuring the rotational diffusion constant while being less affected by larger NP contaminants. To the best of our knowledge, we show here for the first time a quantitative analysis of the rotational diffusion constant of AuNRs in aqueous solution using one-photon luminescence correlation spectroscopy. To correctly apply luminescence correlation spectroscopy to the measurement of the rotational and translational diffusion constants of gold NPs, we therefore first investigated in detail the mechanism of one-photon luminescence

in AuNSs and AuNRs using polarization sensitive single particle spectroscopy in combination with correlated scanning electron microscopy (SEM). Both 514 and 633 nm excitation were employed to distinguish between excitation of the transverse and longitudinal plasmon resonances of the AuNRs. Luminescence correlation spectroscopy was then used to determine the hydrodynamic radii of AuNSs and AuNRs with different sizes in aqueous solution. Sizes measured by correlation spectroscopy were independently checked with transmission electron microscopy (TEM). For all single particle and correlation spectroscopy experiments, one-photon luminescence was compared to plasmon scattering, which has been the most frequently used characterization method of noble metal NPs with single particle sensitivity.

## MATERIALS AND METHODS

**Correlation Spectroscopy Analysis.** Correlation spectroscopy relies on intensity fluctuations within an observation volume to determine the diffusion constant and hydrodynamic radius of molecules or NPs.<sup>42,56,57</sup> Intensity autocorrelation analysis is most commonly applied.<sup>8,12–14,24,50,51</sup> Assuming the presence of only one analyte of interest in the sample, a Gaussian beam-shaped observation volume, and only translational diffusion, the autocorrelation,  $G_D$ , as a function of lag time,  $\tau$ , can be expressed in terms of the observation volume parameters—volume,  $V_{\text{eff}}$  beam waist,  $r_0$ , and beam height,  $z_0$ —mean transient time through the detection volume,  $\tau_D$ , and analyte concentration,  $\langle C \rangle^{39,41}$

$$G_D(\tau) = \frac{1}{V_{\text{eff}} \langle C \rangle} \cdot \frac{1}{\left(1 + \frac{\tau}{\tau_D}\right)} \cdot \frac{1}{\left(1 + \left(\frac{r_0}{z_0}\right)^2 \left(\frac{\tau}{\tau_D}\right)\right)^{1/2}} \quad (1)$$

The mean transient time,  $\tau_D$ , is in turn related to the translational diffusion constant,  $D_{\text{tr}}$ , according to<sup>39,41</sup>

$$\tau_D = \frac{r_0^2}{4D_{\text{tr}}} \quad (2)$$

The hydrodynamic radius,  $R_h$ , is then obtained through the Stokes–Einstein relationship<sup>39,41</sup>

$$D_{\text{tr}} = \frac{k_B T}{6\pi\kappa R_h} \quad (3)$$

where  $k_B$  is the Boltzmann constant,  $T$  the temperature, and  $\kappa$  the viscosity of the solvent. The hydrodynamic radius recovered following this analysis yields an average size for the NPs present in the solution. If the brightness of the NP, i.e., scattering or luminescence intensity, depends on its size, then the contribution to the autocorrelation,  $G_i(\tau)$ , from each species having a different size is weighted by its concentration,  $\langle C_i \rangle$ , and brightness,  $\eta_i$ :<sup>42</sup>

$$G(\tau) = \frac{\sum \eta_i^2 \langle C_i \rangle^2 G_i(\tau)}{(\sum \eta_i \langle C_i \rangle)^2} \quad (4)$$

Deriving the equation to describe the rotational component of the autocorrelation function is more complex involving several assumptions about the relative time scales of the intrinsic signal decay and rotational relaxation, the geometry of the setup, and

the relative orientations of the absorption and emission dipoles. Aragon and Pecora<sup>40</sup> and later Kask et al.<sup>58</sup> developed a model describing the rotational component of the autocorrelation function for correlation spectroscopy experiments assuming rigid particles with collinear absorption and emission dipoles. Based on this model, the rotational autocorrelation function for a perfect dipole,  $G_R$ , is given by<sup>58</sup>

$$G_R(\tau) = \sum_l B_l(\hat{a}, \hat{e}_1, \hat{e}_2) \exp[-l(l+1)D_{rot}\tau] \quad (5)$$

where  $D_{rot}$  is the rotational diffusion constant and  $l$  is the index of the angular momentum eigenvalue and can take values of 0, 2, and 4.  $B_l(\hat{a}, \hat{e}_1, \hat{e}_2)$  are the coefficients calculated for different relative orientations of excitation polarization,  $\hat{a}$ , and two detection polarizations,  $\hat{e}_1$  and  $\hat{e}_2$ . For the autocorrelation function, the signal from a single detector is used and the detection polarizations are the same. For the cross-correlation function, the polarization of  $\hat{e}_1$  and  $\hat{e}_2$  can be different. Note that eq 5 is independent of the focal volume parameters.

It was shown that the rotational component can be reduced to a single exponential when a high numerical aperture (NA) objective is used, as was the case in our setup, where NA = 1.3 (Zeiss Fluar).<sup>24,59</sup> We compared our experimental data to single and multiple exponentials fits and found that single exponentials fits were more consistent.

To relate rotational diffusion constants recovered from correlation spectroscopy measurements to the size of the AuNRs, we used the model by Tirado et al.<sup>23</sup> derived for short cylinders, which describes rotational and translational diffusion of rods:

$$D_{rot} = \frac{3k_B T}{\pi \kappa L^3} \left[ \ln\left(\frac{L}{d}\right) + \sigma \right] \quad (6)$$

$$D_{tr} = \frac{k_B T}{3\pi \kappa L} \left[ \ln\left(\frac{L}{d}\right) + \nu \right] \quad (7)$$

Here,  $L$  and  $d$  are the rod length and diameter, respectively, with  $\sigma$  and  $\nu$  given by  $\sigma = -0.662 + 0.917(d/L)^2 - 0.05(d/L)^4$  and  $\nu = 0.312 + 0.565(d/L) - 0.1(d/L)^2$ .

By equating eq 3 and eq 7 the relationship between the rod dimensions and the hydrodynamic radius can be extracted according to

$$R_h = \frac{L}{2 \ln\left(\frac{L}{d}\right) + \nu} \quad (8)$$

The overall equation for the autocorrelation function including rotational and translational terms is then given by<sup>24,58</sup>

$$\begin{aligned} G(\tau) &= G_D(\tau)G_R(\tau) \\ &= \frac{1}{V_{eff}\langle C \rangle} \cdot \frac{1}{\left(1 + \frac{\tau}{\tau_D}\right)} \cdot \frac{1}{\left(1 + \left(\frac{r_0}{z_0}\right)^2 \left(\frac{\tau}{\tau_D}\right)\right)^{1/2}} \\ &\cdot (1 + A \cdot B_l \cdot \exp(-6D_{rot}\tau)) \end{aligned} \quad (9)$$

The parameter  $A$  is introduced to account for the anisotropy of a real system, which can be different from 1. The same equations given above also apply to cross-correlation measurements with more than one detector and can be used for both scattering and luminescence correlation spectroscopy experiments.

**Correlation Spectroscopy Setup.** Correlation spectroscopy experiments were performed on a home-built instrument based on an inverted Zeiss microscope described previously.<sup>7,56</sup> Excitation was carried out using the 514 nm line of an Ar<sup>+</sup> laser (Modu-Laser) and a 633 nm He–Ne laser (JSD Uniphase). To avoid sampling NP diffusion at the interface and to minimize reflected light from the glass coverslips, the lasers were focused about 4 and 7 μm deep inside the sample chamber for luminescence and scattering correlation measurements, respectively. For luminescence correlation spectroscopy experiments, light collected from the sample was passed through a dichroic mirror and a notch filter (z532rdc, Chroma Technology, and RNF-514.5, CVI, for 514 nm excitation and z633rdc, Chroma Technology, and RNF-632.8, CVI, for 633 nm excitation), which were used to ensure that all excitation light was removed from the signal. No other filters were used, and therefore spectrally integrated intensities were collected for the luminescence correlation measurements. To switch from luminescence to scattering correlation spectroscopy, the dichroic mirror was switched to a 50/50 beam splitter and the notch filter was removed. Sample preparation for correlation measurements was carried out according to procedures published previously.<sup>56</sup>

It is necessary to correctly determine the observation volume parameters in eq 1 in order to calculate diffusion constants and hydrodynamic radii from the measured diffusion times.<sup>42,56,60</sup> This is typically accomplished by correlation spectroscopy with particles of known size. We used solutions of 100 and 200 nm beads (Invitrogen) to separately calibrate the focal volume parameters for scattering and luminescence. The 100 nm beads were used for 514 nm excitation, while the 200 nm beads were used for 633 nm excitation. Figure S1 shows the autocorrelation data of the beads for all four configurations, and Table S1 summarizes the extracted focal volume parameters, which were used for the analysis of the measured NP diffusion times. The larger beads were employed here instead of smaller organic dyes because they also scattered efficiently and could therefore be used to determine the focal volume parameters for the scattering correlation experiments. However, we also independently checked the focal volume parameters by measuring the dye Alexa 555 (Invitrogen) with 514 nm excitation. As illustrated by the corresponding data in Figure S2 and Table S2, comparable values were obtained.

A power dependence study was performed for both scattering and luminescence conditions in order to find the appropriate range of laser powers required to avoid effects of optical trapping or detector saturation. Because the luminescence is much weaker compared to scattering, powers used for luminescence correlation spectroscopy were orders of magnitude higher: ~15 kW/cm<sup>2</sup> for luminescence correlation spectroscopy and ~15 W/cm<sup>2</sup> for scattering correlation spectroscopy, corresponding to values measured at the sample. Pure solvent samples were measured using similar excitation powers to make sure that the signal originates only from the NPs in question. Each sample was measured at least three independent times to yield mean values and corresponding errors.

To ensure that the different excitation powers did not lead to a difference in measured diffusion constants due to a change in local solvent viscosity caused by NP heating, we estimated the increase in temperature at the NP surface. As illustrated in the Supporting Information, the temperature changes due to laser heating for the ranges of excitation powers used in the scattering and luminescence correlation measurements were  $\Delta T_{scattering} \approx$

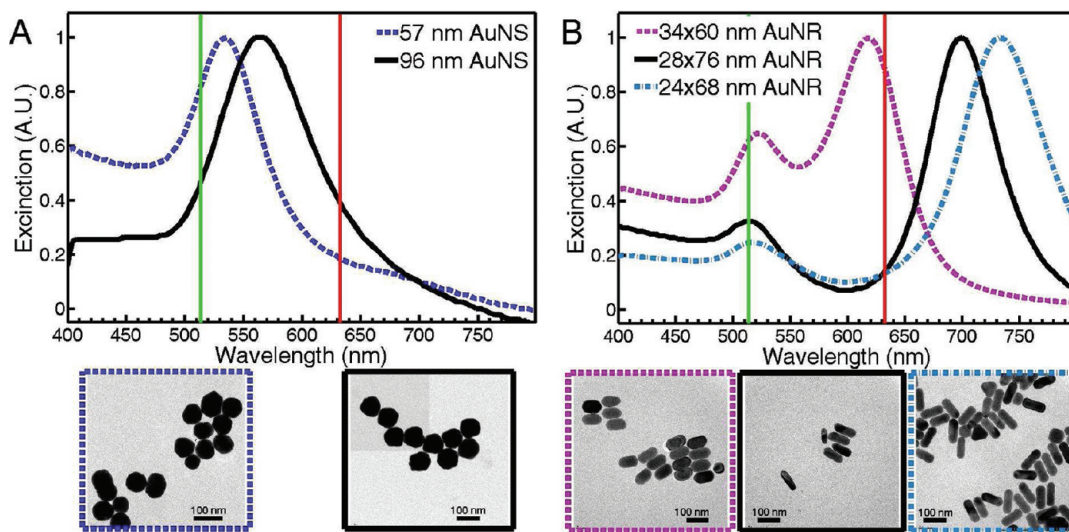


**Figure 1.** UV–vis spectra and TEM images for (A) AuNS samples and (B) AuNR samples used in this study. Vertical lines denote the two excitation wavelengths that we used: 514 nm (green) and 633 nm (red). Representative TEM images for each sample are also included.

0.0002–0.002 K and  $\Delta T_{\text{luminescence}} \approx 0.2\text{--}2$  K. For these values, the resulting changes in solvent viscosity are insignificant to alter the measured diffusion times within the experimental error.

**Polarization Geometry.** The samples were excited with linearly polarized light, and two avalanche photodiode detectors (PerkinElmer) were set up to collect light polarized parallel and perpendicular to the excitation polarization. The propagation direction of the laser light was set along the  $z$ -axis, and the  $x$ -axis was chosen to be parallel to the excitation polarization. The two detectors were then set up to collect light polarized along the  $x$ - and  $y$ -axis. Figure S3 shows a schematic diagram of the experimental setup. Following the convention used by Tsay et al.,<sup>24</sup> we considered three configurations: two autocorrelations with detection polarization parallel and orthogonal to the excitation polarization (XXX and XYY where the first letter denotes the excitation polarization) and one cross-correlation of the signal from the two detectors (XXY). Cross-correlation curves can be calculated as either XXY or XYX, but in all of our experiments XXY and XYX looked identical, and we therefore show only data for XXX.

**Single Particle Spectroscopy.** Single particle spectra were acquired using the same instrument. For scattering spectra, a halogen lamp was used for excitation in a dark-field geometry, and the scattered light was redirected to a spectrometer equipped with a CCD camera (Princeton Instruments PIXIS 400BR). For luminescence spectra, the same laser lines were used for excitation as for the correlation spectroscopy experiments, and the luminescence, collected in an epi-illumination geometry, was sent to the same spectrometer. As needed, specific polarizations of the incident and emitted light were controlled by half-wave plates and placing a polarizer in the detection light path. Unless otherwise specified a polarizer angle of  $\theta = 0$  selects the polarization direction that is parallel to the laboratory  $x$ -axis. A 100X Zeiss Epiplan objective was used to collect all spectra. Correlation between single particle spectra and the dimensions of the NPs was accomplished using a patterned substrate for identification in the optical setup and a SEM (FEI Quanta 400 ESEM FEG) as previously described.<sup>45,61,62</sup>

**Nanoparticle Characterization.** AuNSs and AuNRs were purchased from Nanopartz and characterized with bulk UV–vis

spectroscopy (Shimadzu UV-3101PC) and TEM (JEOL 2010), as shown in Figure 1. This allowed us to quantify the extent of size and shape heterogeneity of these AuNS and AuNR samples. The UV–vis spectra in Figure 1A show single plasmon peaks for the 57 nm (dashed blue line) and 96 nm (solid black line) AuNSs at 535 and 564 nm, respectively. The AuNRs in Figure 1B exhibit two well-defined plasmon peaks in their extinction spectra. The spectral position of the longitudinal plasmon resonance depends mainly on the aspect ratio of the AuNRs for this particular size regime.<sup>63</sup> The maximum of the longitudinal plasmon resonance is at 620 nm for the 34 × 60 nm AuNR sample (dashed purple line), at 700 nm for the 28 × 76 nm AuNR sample (solid black line), and at 735 nm for the 24 × 68 nm AuNR sample (dashed blue line). The samples are labeled according to their mean dimensions. Representative TEM images for these samples are given in Figure 1, while the analysis of the size distributions for each sample is provided in the Supporting Information (Figure S4).

## RESULTS AND DISCUSSION

To measure the rotational diffusion of NPs with correlation spectroscopy using polarized excitation and detection, the polarization of the measured signal needs to be first understood for a stationary NP. While plasmon scattering in AuNRs is polarized along the long rod axis for the longitudinal mode and polarized in the perpendicular direction for the transverse mode, only a few studies exist on one-photon luminescence of gold NPs,<sup>46–49,52–55,64</sup> and the mechanism is still a subject of debate. Two general explanations have been proposed. One mechanism hypothesizes that the luminescence is due to interband electron–hole pair recombination, which is enhanced by the spectrally overlapping plasmon field.<sup>48,52–54,64</sup> The other explanation is that the luminescence is caused by the radiative decay of a plasmon.<sup>47</sup> To quantify the polarization dependence of the luminescence but also to gain a deeper insight into the mechanism, we correlated the spectroscopy of individual gold NPs with their size and orientation using SEM. This approach takes the effects due to

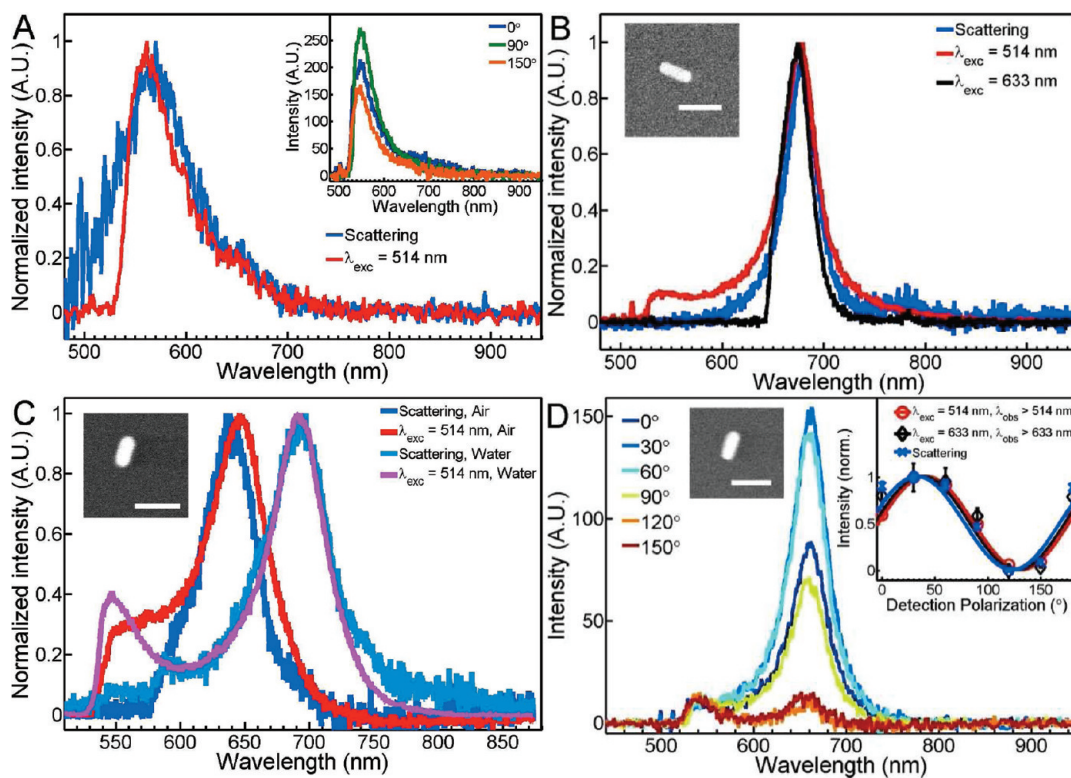


**Figure 2.** (A) Unpolarized scattering (blue) and 514 nm excited luminescence (red) spectra of a 45 nm diameter AuNS. The inset shows polarized luminescence spectra that change in amplitude as the detection polarization was varied. (B) Unpolarized scattering (blue) and luminescence spectra excited at 514 nm (red) and 633 nm (black) of a 27 × 75 nm AuNR shown in the inset. (C) Unpolarized scattering (blue and cyan) and 514 nm excited luminescence (red and magenta) spectra of a 33 × 70 nm AuNR shown in the SEM image, which was immobilized on a glass coverslip and surrounded by air and water, respectively. (D) Polarized luminescence spectra with 514 nm excitation of a 34 × 68 nm AuNR shown in the SEM image. The inset illustrates the intensity as a function of detected polarization obtained by integrating the area under the spectra for the corresponding entire spectral ranges and then normalized to the maximum value, for luminescence excited at 514 nm (red) and 633 nm (black) as well as for scattering (blue). The error bars were computed from at least three spectra that were acquired for each polarization. The excitation light is unpolarized and circularly polarized for the scattering and luminescence spectra, respectively. All scale bars correspond to 100 nm.

size and shape heterogeneity directly into account while eliminating the possibility that the signal is caused by other luminescent impurities. Interestingly, we were unable to observe luminescence in bulk measurements with lamp excitation. Because of the high excitation rate in the single particle measurements using a laser excitation source, enough signal could, however, be collected for recording single particle spectra. Dichroic mirrors and notch filters were placed in the detection beam path to ensure that the more intense scattered excitation light was blocked out.

For a single AuNS the luminescence follows the scattering spectrum and shows a weak polarization dependence. The AuNSs are not perfect spheres and interact with light differently depending on their orientation relative to the incident light polarization as was observed previously for single particle scattering and absorption.<sup>45,65,66</sup> Figure 2A compares the scattering and the luminescence spectra, excited by a lamp (500–1000 nm) and with a 514 nm laser, respectively, for the same AuNS that was also imaged by correlated SEM. The size of the AuNS was 45 nm (Figure S5). The luminescence spectra vary with the detected polarization angle, as shown in the inset of Figure 2A.

The luminescence spectra of the AuNRs are independent of the excitation wavelength. For the single AuNR, shown in the SEM image in the inset of Figure 2B, unpolarized spectra of

scattering, 514 nm, and 633 nm excited luminescence are displayed in the main part of Figure 2B. The three spectra are almost indistinguishable from each other for the longitudinal plasmon resonance. Thus we can conclude that these spectra excited at a single laser wavelength are indeed due to luminescence and not elastic scattering and also that luminescence can be excited both at the transverse (514 nm) or the longitudinal (633 nm) plasmon resonance giving nearly identical responses that spectrally overlap with the longitudinal plasmon band. The luminescence spectrum, when excited at 514 nm, also has a peak near 520 nm that coincides with the transverse plasmon resonance, which is visible in the bulk extinction spectrum, but too weak to be seen in the single particle scattering spectra.<sup>25</sup> The exact location of this short wavelength peak cannot be determined because of the dichroic filter that was used.

To investigate if the luminescence is caused by the absorption of one or multiple photons, we carried out a power dependence of the luminescence intensity. Figure S6 shows that the luminescence intensity indeed scales linearly with laser power for AuNRs excited at 514 and 633 nm, confirming a one-photon excitation process. It is also important to note that the luminescence from immobilized AuNRs does not show any signs of intensity blinking, which is illustrated in Figure S7.

The luminescence spectrum shifts with a change of the dielectric constant of the surrounding medium in the same way

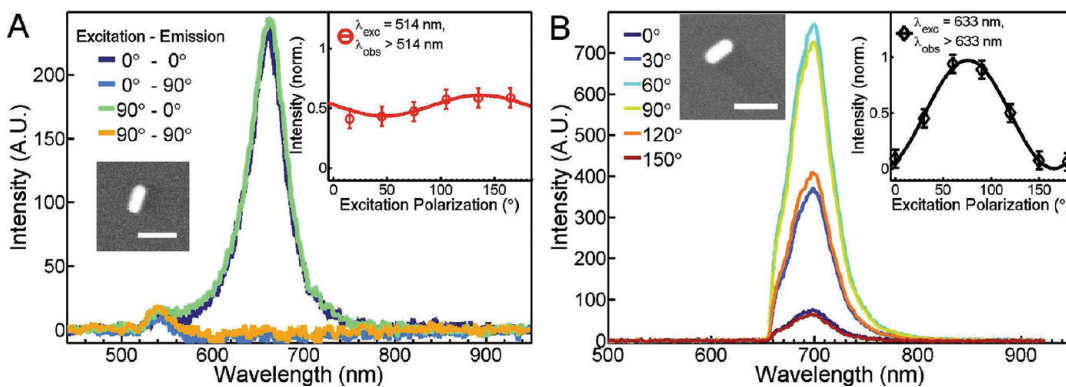


**Figure 3.** (A) Luminescence spectra of a  $34 \times 68$  nm AuNR excited at  $514\text{ nm}$  taken at varying orientations of excitation and detection polarizations relative to the long axis of the AuNR. The integrated intensity as a function of excitation polarization is given in the inset. For this data the detection polarizer was removed. For this experiment only, the reported angles are defined with respect to the long axis of the AuNR. (B) Unpolarized luminescence spectra of a  $35 \times 72$  nm AuNR shown in the SEM image excited at  $633\text{ nm}$  for different excitation polarizations. The integrated intensity as a function of excitation polarization is shown in the inset. All scale bars correspond to  $100\text{ nm}$ .

as the scattering spectrum. Figure 2C shows single particle scattering (blue and cyan) and  $514\text{ nm}$  excited luminescence (red and magenta) spectra for a  $33 \times 70$  nm AuNR supported on glass taken in air and water, respectively. The effective refractive index changes from  $\sim 1.25$  as in the case of the spectra taken in air, to 1.4 for the spectra taken with water on top of the sample. The shift in the resonance maximum is about  $50\text{ nm}$  for both scattering and luminescence. The transverse plasmon resonance did not shift measurably but is resolved better in the luminescence spectrum with the added water because the shoulder of the longitudinal resonance no longer overlaps significantly. These results suggest that the observed luminescence is caused by emission of a plasmon. This mechanism can be probed in more detail by studying the polarization dependence of the luminescence excited at  $514$  and  $633\text{ nm}$ .

The polarized luminescence spectra of a single  $34 \times 68$  nm AuNR in Figure 2D show a strong polarization dependence for the longitudinal mode which modulates in phase with the scattering signal. In contrast, the short wavelength peak is only weakly polarization dependent. To calculate the modulation depth of the scattering and luminescence intensity as a function of the detection polarization, we recorded spectra for 10 different AuNRs as a function of polarizer angle and integrated the entire area under the spectra for each of them. An example for scattering and luminescence of the same AuNR is shown in the inset of Figure 2D. The resulting polarization traces were fit to  $I(\theta) = N(1 + M \cos 2(\theta - \varphi))$ , where  $N$  is a normalization factor,  $M$  is the modulation depth,  $\theta$  is the polarizer angle, and  $\varphi$  represents the angle of the longest projected dipole axis with respect to a reference frame.<sup>28</sup> Scattering exhibits a perfect dipole behavior with an average modulation depth of  $0.95 \pm 0.05$  obtained from 10 individual AuNRs. Luminescence for  $633\text{ nm}$  excitation closely follows amplitude and phase of scattering, and its modulation depth is  $0.94 \pm 0.05$ . The integrated luminescence for  $514\text{ nm}$  excitation has a slightly lower modulation depth of  $0.90 \pm 0.07$  because the short wavelength peak does not change in amplitude for different detection polarizations.

In addition to the emission dipole, the polarization of the absorption dipole is also important to understand the correlation spectroscopy measurements. We therefore probed it by recording spectra as a function of the excitation polarization. We found that the longitudinal plasmon luminescence is independent of

the excitation polarization at  $514\text{ nm}$  and always occurs along the long axis of the AuNR. This was determined by independently controlling the polarization angles of both excitation and detection as shown in Figure 3A. When the excitation is set parallel to the short axis of the AuNR and the detected polarization is parallel to the long AuNR axis, the highest intensity is obtained ( $90^\circ - 0^\circ$ , green). No changes are observed when the excitation polarization is rotated by  $90^\circ$  ( $0^\circ - 0^\circ$ , dark blue). On the other hand, rotating the emission polarizer by  $90^\circ$  erases the longitudinal peak independent of the excitation polarization. Therefore, we can conclude that luminescence of the AuNR is always aligned parallel to the long axis, regardless of the excitation polarization. The independence of the excitation polarization is further illustrated in the inset of Figure 3A, where the unpolarized integrated luminescence intensity is plotted as a function of excitation polarization yielding an almost negligible modulation depth.

Excitation at  $633\text{ nm}$ , on the other hand, exhibits the expected pure dipole behavior and matches the phase of the luminescence. Therefore absorption and emission dipoles are collinear for  $633\text{ nm}$  excitation. Unpolarized luminescence spectra of a  $35 \times 72$  nm AuNR for different excitation polarizations are shown in Figure 3B. Plotting the integrated area under the spectra versus the excitation polarization yields the curve shown in the inset of Figure 3B and a modulation depth of 0.97 confirming a perfect dipole behavior.

We assign the luminescence to the radiative decay of surface plasmons. Figure 4 shows a suggested mechanism for one-photon plasmon emission of AuNRs. Luminescence occurs from both the transverse and longitudinal surface plasmon resonances with the latter being the dominant decay channel. This model is supported by the nearly perfect spectral overlap of the luminescence with scattering in both air and water environments and the high polarization dependence of the longitudinal surface plasmon emission. The spectral overlap between scattering and luminescence observed here and the suggested mechanism are consistent with a previous ensemble study on the one-photon luminescence of AuNSs<sup>47</sup> as well as two-photon luminescence recorded from individual AuNRs.<sup>17</sup>

The observation that the emission of the AuNSs also follows the plasmon resonance validates the assignment of the short wavelength peak in the AuNR luminescence spectrum to

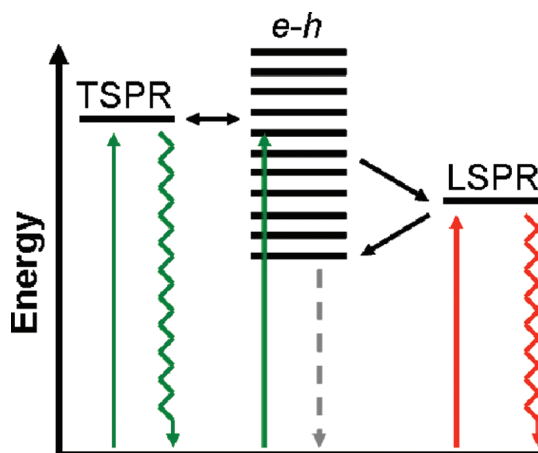


**Figure 4.** Schematic diagram of the mechanism for one-photon plasmon luminescence of AuNRs. The solid green lines represent excitation with 514 nm laser light, which excites both d-sp interband transitions creating electron–hole ( $e-h$ ) pairs and the transverse surface plasmon resonance (TSPR). The solid red line depicts excitation of the longitudinal surface plasmon resonance (LSPR) with 633 nm laser light. The wavy green and red lines represent emission from the TSPR and LSPR, respectively. Nonradiative relaxation occurs through recombination of  $e-h$  pairs as indicated by the dashed gray line. For simplicity no distinction is made in this diagram between  $e-h$  pairs excited by interband vs intraband transitions. Furthermore, note that the threshold for interband transitions lies above the LSPR.

emission of the transverse plasmon. At 514 nm, both d-sp interband transitions and the transverse surface plasmon are excited due to their spectral overlap. Interband absorption creates electron–hole pairs that can relax very efficiently through nonradiative pathways because of the large density of states in the sp-conduction and d-valence bands. However, analyzing the excitation and emission polarizations of the short wavelength peak in the AuNR luminescence spectra revealed a significant depolarization of the emission compared to previous polarization sensitive photothermal imaging of the absorption at 514 nm.<sup>28</sup> This loss of polarization is assigned to a fast interconversion between electron–hole pairs and the transverse surface plasmon resonance that subsequently decays radiatively. Because of the limited spectral range for the transverse mode due to the dichroic used, other luminescence mechanisms like plasmon-amplified electron–hole pair recombination<sup>48,52–54</sup> cannot be completely ruled out for this wavelength range. In contrast, 633 nm corresponds to energies below the interband absorption threshold, and hence radiative recombination between d-valence band holes and sp-conduction band electrons should not be possible. At a wavelength of 633 nm, direct excitation of the longitudinal surface plasmon resonance occurs as illustrated in Figure 4. Because of the large bandwidth of the plasmon resonance, excitation at the blue edge is possible and emission occurs within the spectral bandwidth of the plasmon resonance so that a distinct Stokes shift as seen in molecular fluorescence is not observed here.

The importance of hot electron–hole pairs and the fast interconversion between them and surface plasmons becomes more evident when considering the longitudinal surface plasmon resonance. Direct excitation at 633 nm is highly polarized parallel to the long AuNR axis for both absorption and emission and leads to either direct plasmon emission or nonradiative decay through the generation of electron–hole pairs. However, excitation

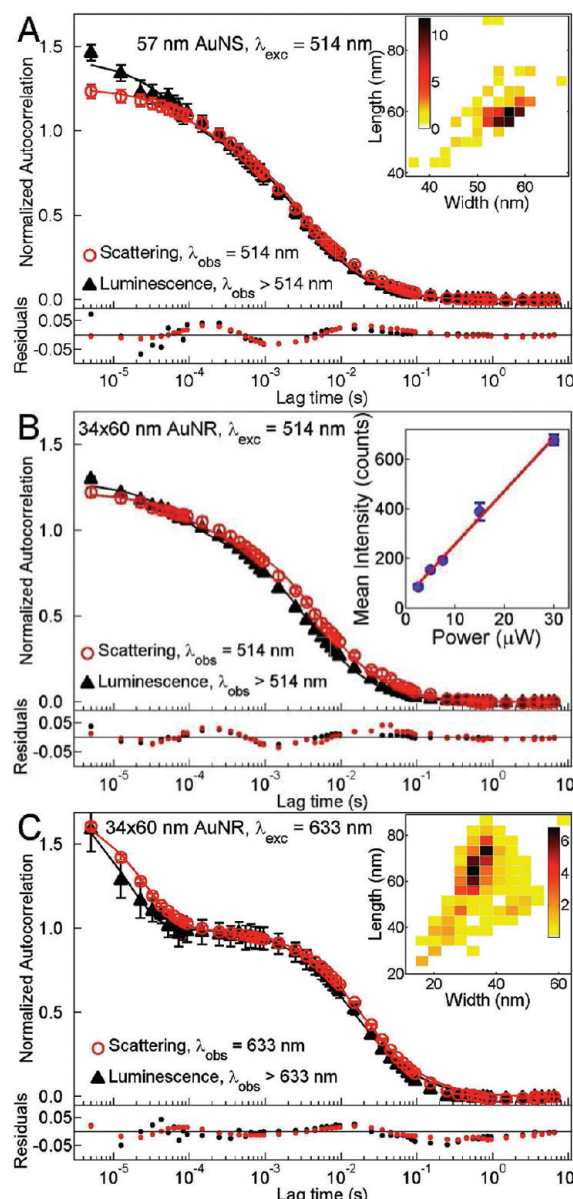


**Figure 5.** Autocorrelation curves from luminescence (black triangles) and scattering (red circles) for 57 nm AuNSs with 514 nm excitation (A), 34  $\times$  60 nm AuNRs with 514 nm excitation (B), and 34  $\times$  60 nm AuNRs with 633 nm excitation (C). The curves are normalized so that the amplitude of the translational component equals 1. Rotational diffusion times and amplitudes and translational diffusion times are listed in Table S3. The luminescence intensity as determined from the raw time transients scales linearly with the excitation power, shown in the inset of (B), which indicates a one-photon process. Size distributions for the 57 nm AuNS and the 34  $\times$  60 nm AuNR samples are shown in the insets of (A) and (C), respectively.

at 514 nm also gives rise to mainly longitudinal surface plasmon emission, which does not depend on the excitation polarization. Because the transverse and longitudinal modes are orthogonal to each other, this observation can only be rationalized if hot electron–hole pairs can also create surface plasmons. The decay of surface plasmons into electron–hole pairs is a well-accepted energy relaxation channel,<sup>25,67</sup> but our results also show that the opposite is possible, although most likely with a much smaller yield.

Estimating a detection efficiency of 5% for our microscope setup, we determined the quantum yields of plasmon emission for different excitation wavelengths.<sup>55</sup> Using calculated absorption cross sections of  $1.44 \times 10^3$  and  $1.87 \times 10^3 \text{ nm}^2$  at 514 and 633 nm for a  $24 \times 76 \text{ nm}$  AuNR, and respective incident laser powers of 37.5 and  $1.5 \mu\text{W}$  (or 13 and  $0.5 \text{ kW/cm}^2$ ) at the sample, luminescence quantum yields of  $8 \times 10^{-6}$  and  $3 \times 10^{-4}$  are obtained for 514 and 633 nm excitation, respectively. Luminescence excited at the longitudinal surface plasmon resonance is significantly more efficient, which can be explained by the fact that the longitudinal surface plasmon energy is below the threshold for interband absorptions. Nonradiative recombination of electrons with holes in the valence band is hence no longer possible, consistent with longer plasmon dephasing times.<sup>25</sup> Most of the energy is, however, dissipated via the nonradiative recombination of electron–hole pairs as shown by the gray line in Figure 4.

We now turn to scattering and luminescence auto- and cross-correlation measurements for different AuNSs and AuNRs. Using the results from the polarization dependence of one-photon luminescence in AuNSs and AuNRs, we can determine their rotational and translational diffusion constants and calculate their hydrodynamic radii. Another important consideration in performing a correlation analysis is the effect of sample heterogeneity on the extracted sizes.<sup>13,14,42,56,68</sup> No NP sample is ever perfectly homogeneous. The size histograms in Figure S4 show that the AuNS samples contain nonspherical NPs and that the AuNR samples include AuNSs. An important question is therefore how sample inhomogeneity affects scattering vs luminescence correlation spectroscopy.

Scattering and luminescence of AuNSs and AuNRs can both be used to study rotational dynamics. As illustrated in Figure 5, scattering and luminescence produce very similar autocorrelation curves for the AuNS and AuNR samples used in the present study. The insets of Figures 5A and 5C depict the size distributions for each sample, as determined from TEM. Scattering and luminescence experiments at two excitation wavelengths (514 and 633 nm) were carried out for the AuNR sample, while only 514 nm excitation was employed for the AuNS sample because of the lack of signal for 633 nm excitation, as expected from the spectra in Figure 1. A linear dependence of the average luminescence intensity on laser power for these correlation measurements, as shown in the inset of Figure 5B, again confirms a one-photon excitation process.

The autocorrelation curves shown in Figure 5 were fit to eq 9, which appears to well describe the luminescence as well as scattering correlation data for both AuNSs and AuNRs. We assign the slower component to translational diffusion, while the faster component is attributed to rotational motion, which is particularly pronounced for the AuNRs. Fast photophysical processes such as blinking can be ruled out as the origin of the faster component as no intensity fluctuations typical of blinking events were observed for plasmon scattering and luminescence (Figure S7). The small fast component also observed for the AuNS sample in Figure 5A can be attributed to deviations from a perfectly spherical shape,<sup>65</sup> consistent with the small anisotropy seen in the single particle luminescence spectra in the inset of Figure 2A.

The autocorrelation curves in Figure 5 were computed using the detector that monitored the polarization component of the signal that was perpendicular to the excitation polarization, denoted XYY, as described in the Methods section and illustrated

in Figure S3. However, we can gain further insight into the rotational diffusion component by also considering the autocorrelation of the other detector that monitors the parallel polarization component (XXX) or the cross-correlation between the two detectors (XXY). These autocorrelation and cross-correlation curves for the  $34 \times 60 \text{ nm}$  AuNR sample are shown in Figures 6A and 6B, for scattering and luminescence excited at 633 nm, respectively, and in Figures 6C and 6D, for scattering and luminescence excited at 514 nm, respectively. As in Figure 5, all curves are normalized so that the amplitude of the translational component is 1. The auto- and cross-correlation traces (symbols) for 633 nm excitation perfectly follow the theoretically predicted trends (dashed lines of matching colors) for a perfect dipole using the model derived by Kask et al.<sup>58</sup> (eq 9). The average recovered value for the anisotropy is  $\sim 0.95$  for both scattering and luminescence, consistent with the behavior of a single dipole. The model describes the data extremely well: the autocorrelation for the detector monitoring polarization parallel to the excitation (XXX, red circles) has the largest amplitude; the autocorrelation for the other detector (XYY, black triangles) and the cross-correlation (XXY, blue crosses) coincide with each other as well as the theoretical curve.

In contrast to 633 nm excitation, the experimental data shown in Figure 6C for scattering correlation spectroscopy with 514 nm excitation cannot be described by the model of Kask et al.<sup>58</sup> even if a variable anisotropy term  $A$  is introduced in eq 9 as suggested by Tsay et al.<sup>24</sup> Theoretically expected auto- and cross-correlation curves for a perfect dipole are shown as dashed lines of the corresponding color to emphasize the difference compared to the results for 633 nm excitation. Fitting of the two autocorrelation curves with a variable anisotropy gave recovered values that were different from each other and hence inconsistent: 0.3 and 0.6 respectively for XXX (red circles) and XYY (black triangles). It is important to note that the fits to the autocorrelation curves in Figure 6C with those anisotropy values are good (Figure S8) and that an erroneous conclusion could have been made about the anisotropy at 514 nm if each detector was considered separately. We therefore hypothesize that the model fails to correctly describe the data because of the cylindrical symmetry of the transverse plasmon mode, which is different from a molecular dipole that is assumed in the model.

Similar to the scattering data, the two luminescence autocorrelations in Figure 6D produce different values for the anisotropy. But unlike the scattering cross-correlation (XXY in Figure 5C), cross-correlation of the luminescence resulted in a cross-correlation intensity that initially rises (XXY in Figure 5D). A rise indicates that the absorption and emission dipoles of the AuNRs are not collinear for 514 nm excitation, consistent with the results shown in Figure 3 obtained by polarization sensitive single particle luminescence spectroscopy. If the directions of the absorption and emission dipoles are different, then a major assumption in the model of Aragon and Pecora<sup>40</sup> and Kask et al.<sup>58</sup> is no longer valid and the coefficients  $B_l(\hat{a}, \hat{e}^1, \hat{e}_2)$  in eqs 5 and 9 can become negative, leading to an initial intensity increase for the rotational component. The observations that the luminescence spectrum of the AuNRs is dominated by the highly polarized longitudinal plasmon resonance and that the luminescence is independent of the excitation polarization when excited at 514 nm can therefore explain the rise in the luminescence cross-correlation curve at early lag times (Figure 6D).

Finally, we need to consider the possibility of photoselection as the reason for the difference between 514 and 633 nm

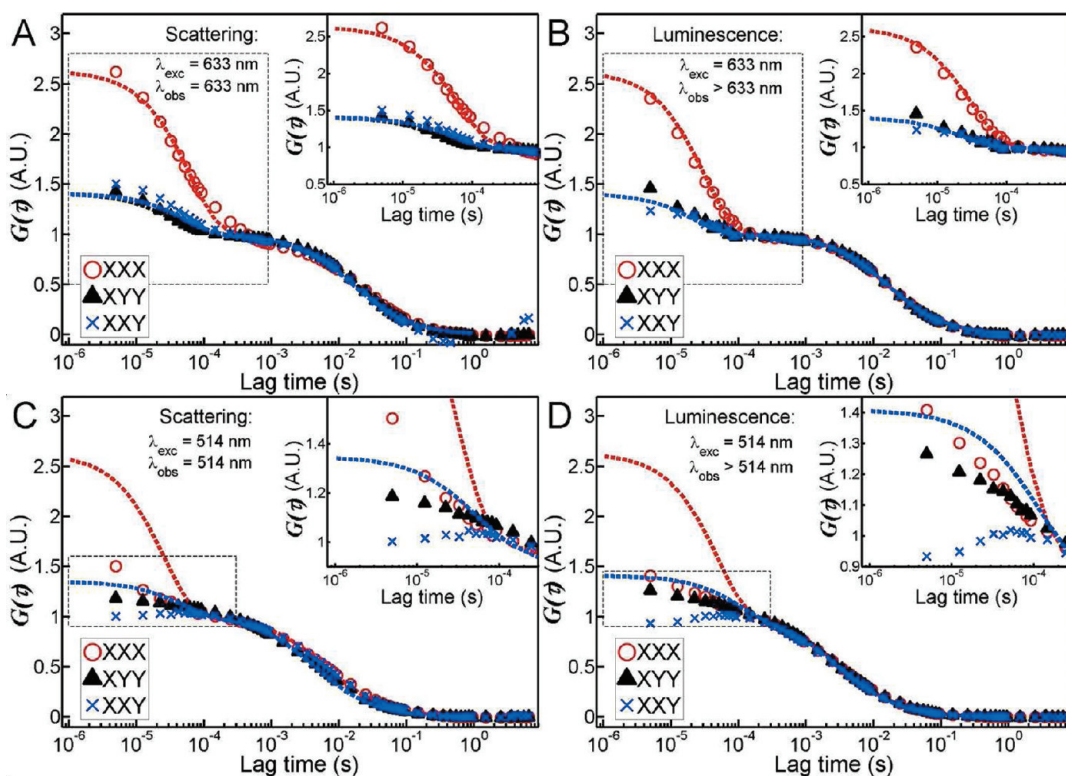


**Figure 6.** Two autocorrelations and one cross-correlation for the  $34 \times 60$  nm AuNR sample with 514 and 633 nm excitation. The first letter of the legend denotes the excitation polarization; second and third letters stand for the detection polarizations (see Materials and Methods for more details). (A) and (B) show scattering and luminescence correlation curves, respectively, excited at 633 nm. Experimental data are given by symbols, and theoretically expected trends for a perfect dipole are shown as dashed lines. (C) and (D) show scattering and luminescence correlation curves, respectively, excited at 514 nm. For this excitation wavelength, however, experimental data do not follow the theoretical trends for a perfect dipole, shown as dashed lines, and moreover scattering and luminescence data are no longer the same. Also note that the luminescence cross-correlation curve has a significant rising edge at short lag times. The curves are normalized so that the amplitude of the translational component equals 1. Rotational diffusion times and amplitudes and translational diffusion times for the different cases are listed in Table S4.

excitation. Scattering at 514 nm by the transverse plasmon of AuNRs is weaker compared to that by AuNSs, which were present in the sample as well. Thus photoselection of AuNSs could also affect the scattering correlation curves. However, using a burst intensity frequency analysis (BIFA), we compared the number of burst events for 514 and 633 nm excitation for the  $34 \times 60$  nm AuNRs sample and found similar values (Figure S9) indicating that the correlation signals in Figures 6C and 5B cannot be due to mainly monitoring AuNSs.

To examine the accuracy of a quantitative analysis of the rotational and translational diffusion, we compared the AuNS and AuNR sizes extracted from scattering and luminescence autocorrelation spectroscopy with those obtained from TEM analysis. The average sizes recovered from each method at the two excitation wavelengths, along with the spread in values collected, are compared in Figure 7. Data for scattering correlation spectroscopy (where the observation wavelength  $\lambda_{\text{obs}}$  equals the excitation wavelength  $\lambda_{\text{exc}}$ , i.e.,  $\lambda_{\text{obs}} = \lambda_{\text{exc}}$ ) are shown as solid symbols, while the results for luminescence correlation spectroscopy (where the observation wavelength  $\lambda_{\text{obs}}$  is red-shifted from the excitation wavelength  $\lambda_{\text{exc}}$ , i.e.,  $\lambda_{\text{obs}} > \lambda_{\text{exc}}$ ) are given by the open symbols. The green and red colors refer to 514 and 633 nm excitation, respectively. In order to show all measurements on the same graph, the results are presented as relative deviations from the expected values based on the NP sizes determined by TEM. The beige rectangles in Figure 7 illustrate the spread of one

standard deviation for each hydrodynamic radius calculated using the TEM size distributions (Figure S4) and eq 8. To compare all NP samples on the same scale, the mean sizes based on the TEM analysis are set to zero and the percentage deviations are shown. The error bars for the correlation spectroscopy data correspond to the standard deviation of at least three independent measurements. Absolute values for the data shown in Figure 7 are also listed in Table S5 together with rotational and translational diffusion times and constants. Although including a rotational diffusion component using eq 9 generally yielded a better fit to the correlation data because of the polarization anisotropy of all NP samples, the rotational diffusion time was only considered for the size analysis of AuNRs when 633 nm was used, as the rotational diffusion component was generally very small for 514 nm excitation and agreement with the model (eqs 5 and 9) was furthermore poor. This leaves us to speculate that the similar amplitudes for the autocorrelation curves for the AuNSs and AuNRs shown in Figure 5A and 5B are likely accidental. In addition, size heterogeneity could be another factor contributing here. However, we verified that fitting only translation diffusion (eq 1) to the data recorded with 514 nm excitation yielded very similar translational diffusion times (Table S5).

The hydrodynamic radius of NPs also includes the organic capping material stabilizing colloidal NPs. However, this was not included in the values calculated from the TEM analysis. The cetyltrimethylammonium bromide (CTAB) coating for the

AuNRs has previously been determined to be 1–3 nm.<sup>69,70</sup> While our correlation spectroscopy results are consistent with this value, the associated error did not allow for an independent quantitative analysis of the CTAB thickness. However, in general we find very good agreement between the average hydrodynamic radii obtained by the different correlation spectroscopy measurements and the sizes determined by TEM. The origin of the error in determining the hydrodynamic radius from correlation spectroscopy as well as the fact that the error appears to vary between methods (scattering vs luminescence and 514 vs 633 nm excitation) will be discussed in more detail next.

As shown in Figure 7, and as reported previously for NPs,<sup>7,13,14,56</sup> sample size heterogeneity affects the results of correlation spectroscopy measurements. This is observed as a broad spread in extracted sizes. However, Figure 7 also shows that, by carefully selecting experimental conditions, the effects of size heterogeneity can be mitigated. In particular for the AuNR samples, 633 nm excitation leads to lower uncertainties in recovered values as compared to 514 nm excitation. Two factors

possibly lead to this difference. The first is the fact that at 514 nm almost all NPs present in these samples have a plasmon resonance and therefore all of them will contribute to the recovered value. Only the AuNRs produced enough signal to be detected for photoselective excitation with 633 nm. The second factor is that the rotational diffusion constant obtained with 633 nm excitation provides a second independent measure of the hydrodynamic radius of the AuNRs. The translational diffusion constant relies only on the calibration of the focal volume parameters, whereas the rotational component requires assumptions about the geometry of the sample and the setup, but is independent of the size of the focal volume. Likewise, assumptions about the rotational diffusion model do not affect the translational component. Therefore combining the results from the two measurements allows us to check for consistency and improve the reliability of the measured values. In addition, recovering similar sizes from the rotational and translational diffusion constants therefore justifies any assumptions made in the data analysis.

We can obtain further information from the data shown in Figure 7. In nearly all samples studied, the NP sizes and standard deviations recovered using scattering correlation spectroscopy are larger than those extracted using luminescence correlation spectroscopy. Because scattering and luminescence strongly depend on NP size and shape,<sup>27,44–47,71</sup> heterogeneity in the NP morphology leads to a distribution of the signal intensity for scattering and luminescence, biasing the recovered hydrodynamic radii toward larger sizes in the correlation spectroscopy experiments.<sup>56</sup> As the scattering intensity scales more strongly with size for AuNSs ( $I \sim V^2$ ) compared to the luminescence intensity ( $I \sim V$ ),<sup>46,47</sup> the presence of larger AuNSs should influence scattering correlation spectroscopy measurements more severely. To test if this is indeed the case here, we compared scattering and luminescence correlation spectroscopy for a mixture comprised of 98% 57 nm and 2% 96 nm AuNSs. Luminescence and scattering autocorrelation curves for 57 and 96 nm AuNSs as well as a mixture of these two samples are shown in Figures 8A and 8B, respectively.

The results in Figure 8 indeed verify that luminescence correlation spectroscopy is not as strongly influenced by the presence of low concentrations of larger NPs compared to scattering correlation spectroscopy, although size heterogeneity still complicates recovering correct hydrodynamic radii because of the size dependent NP brightness. Strikingly, the mixture of 57 and 96 nm AuNSs (green circles) looks indistinguishable from

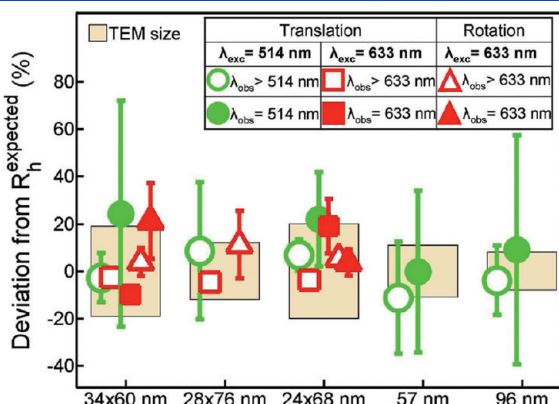


**Figure 7.** Recovered hydrodynamic radii  $R_h$  for the five different samples used in this study are shown as deviations from the values that are expected based on the TEM measurements. Data for scattering correlation spectroscopy ( $\lambda_{obs} = \lambda_{exc}$ ) are shown as solid symbols; luminescence correlation spectroscopy ( $\lambda_{obs} > \lambda_{exc}$ ) results are given by the open symbols. Green and red colors refer to 514 and 633 nm excitation, respectively. Values recovered from rotational components of the autocorrelation curves are shown as triangles. Only 633 nm excitation was considered for the analysis of the rotational diffusion because of the reasons given in the text. The size heterogeneity determined by TEM is indicated by the beige rectangles.

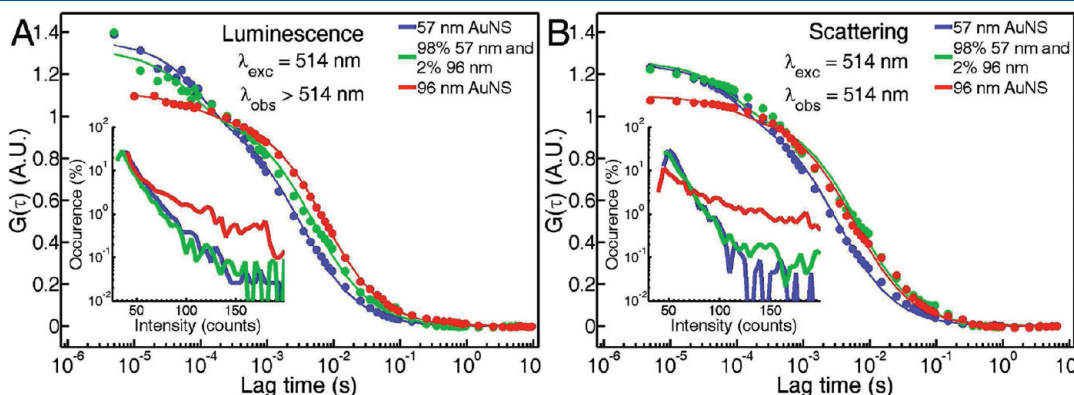


**Figure 8.** Luminescence (A) and scattering (B) autocorrelation curves of 57 nm AuNSs (blue), 96 nm AuNSs (red), and their mixture (green), consisting of 98% 57 nm and 2% 96 nm AuNSs. Insets show intensity histograms constructed by BIFA for each sample.

the pure 96 nm AuNSs (red circles) for the scattering experiments in Figure 8B. In contrast, the size recovered for the mixture using luminescence correlation spectroscopy in Figure 8A falls in between 57 and 96 nm, therefore indicating that larger AuNSs do not completely overwhelm the signal from the 57 nm AuNSs (blue circles). Based on this data, we can conclude that luminescence correlation spectroscopy is advantageous over scattering correlation spectroscopy because the former is not as strongly affected by the presence of a small percentage of aggregates or larger NPs.

We have shown previously that BIFA of the signal transients is a powerful way to gain more insight into the composition of NP mixtures.<sup>7</sup> Intensity histograms constructed by BIFA are shown in the insets of Figures 8A and 8B. For both luminescence (Figure 8A inset) and scattering (Figure 8B inset), the intensity histograms of the pure AuNS samples (blue and red lines) are clearly different from each other. Average blip intensities for pure 57 and 96 nm AuNSs are  $48 \pm 1$  and  $75 \pm 3$  respectively for luminescence and  $58 \pm 1$  and  $140 \pm 20$  for scattering. The intensity histogram of the mixture (green line) is virtually indistinguishable from that of the 57 nm AuNSs (blue line) for both scattering and luminescence, which is in agreement with the very small percentage of 96 nm AuNSs present in the mixture.

## CONCLUSIONS

By recording single particle luminescence spectra using polarization sensitive excitation and detection, we found that one-photon luminescence of AuNSs and AuNRs closely follows the scattering spectrum. Regardless of the excitation wavelength the major intensity of the luminescence always occurs polarized along the long axis of the AuNRs through emission of longitudinal plasmons, which can only be explained by fast interconversion between hot electron–hole pairs and surface plasmons. For 514 nm excitation, transverse surface plasmons and interband absorption create hot electron–hole pairs that subsequently decay into longitudinal plasmons causing an apparent depolarization of the absorption dipole moment. These luminescence results therefore reveal the important interplay between hot electron–hole pairs and surface plasmons, which could be exploited for plasmon-assisted surface photochemistry. We have shown that, with this knowledge about the mechanism of one-photon luminescence, luminescence correlation spectroscopy can be used to measure the unconstrained Brownian motion of AuNSs and AuNRs in solution and recover correct NP sizes. We confirmed that luminescence correlation spectroscopy is less sensitive to aggregation than scattering correlation spectroscopy, in agreement with the weaker NP size dependence of luminescence compared to scattering, and as such could potentially be used for environments that trigger aggregation of NPs (e.g., high ionic strength). For AuNRs, we further determined that direct excitation at the longitudinal surface plasmon resonance at 633 nm is better suited to study the rotational diffusion, because the absorption and emission dipoles are collinear, which improves the amplitude of the rotational component. Absorption and emission dipoles for luminescence excited at 514 nm are not collinear, which causes the theoretical equations that model the auto- and cross-correlation functions to break down. Considering all these factors, the most consistent results compared to independent TEM size characterization were obtained by analyzing both rotational and translational diffusion times for AuNRs recorded with luminescence correlation

spectroscopy using 633 nm, exciting the strongly polarized longitudinal surface plasmon resonance. To measure small changes in hydrodynamic radii of AuNRs due to surface binding of molecules, rotational diffusion times recovered from luminescence correlation curves are expected to be most sensitive, which will be addressed in future studies. For efficient screening of different AuNR samples, 514 nm excitation and analysis of only the translational diffusion component is, however, very useful because all AuNRs independent of aspect ratio can be excited.

## ASSOCIATED CONTENT

**S Supporting Information.** Temperature change at the NP surface, calibration of the focal volume parameters, diagram of the experimental setup, sample size distributions, SEM image of the AuNS shown in Figure 2A, luminescence intensity as a function of laser power for AuNRs, luminescence transient from a single AuNR, fitting of XXX and XYY autocorrelation functions of AuNRs excited at 514 nm, BIFA analysis of AuNRs excited at 514 and 633 nm, and tables containing the translational and rotational diffusion times and amplitudes for Figures 5 and 6 as well as a table summarizing the diffusion-related data from all samples measured. This material is available free of charge via the Internet at <http://pubs.acs.org>.

## AUTHOR INFORMATION

### Corresponding Author

\*E-mail: cflandes@rice.edu (C.F.L); slink@rice.edu (S.L.).

### Author Contributions

<sup>†</sup>These authors contributed equally.

## ACKNOWLEDGMENT

This work was supported by the Nanoscale Science and Engineering Initiative of the National Science Foundation under NSF Award Numbers EEC-0647452 and CHE-0955286, the Robert A. Welch Foundation (Grant C-1664 to S.L.), the ACS Petroleum Research Fund (50191-DNI6), and a 3M Nontenured Faculty Grant. W.-S.C. acknowledges support from the Richard E. Smalley Institute for a Peter and Ruth Nicholas fellowship. P.S. acknowledges support from the Royal Thai Government, and L. S.S. thanks the NSF IGERT Nanophotonics fellowship program. C.F.L. thanks the Norman Hackerman Welch Young Investigator Program at Rice University and the Donors of the American Chemical Society Petroleum Research Fund for partial support of this research. We thank Prof. James Tour for allowing us to use his absorption spectrometer, and Saumyakanti Khatua for assistance with acquiring the single particle spectra. We also thank Profs. Naomi Halas, Peter Nordlander, and Carsten Sönnichsen for insightful discussions.

## REFERENCES

- (1) Hirsch, L. R.; Stafford, R. J.; Bankson, J. A.; Sershen, S. R.; Rivera, B.; Price, R. E.; Hazle, J. D.; Halas, N. J.; West, J. L. *Proc. Natl. Acad. Sci. U.S.A.* **2003**, *100*, 13549–13554.
- (2) Huang, X. H.; El-Sayed, I. H.; Qian, W.; El-Sayed, M. A. *J. Am. Chem. Soc.* **2006**, *128*, 2115–2120.
- (3) Kang, B.; Mackey, M. A.; El-Sayed, M. A. *J. Am. Chem. Soc.* **2010**, *132*, 1517–1519.

- (4) Quarta, A.; Di Corato, R.; Manna, L.; Argentiere, S.; Cingolani, R.; Barbarella, G.; Pellegrino, T. *J. Am. Chem. Soc.* **2008**, *130*, 10545–10555.
- (5) Lee, H.; Yu, M. K.; Park, S.; Moon, S.; Min, J. J.; Jeong, Y. Y.; Kang, H. W.; Jon, S. *J. Am. Chem. Soc.* **2007**, *129*, 12739–12745.
- (6) Nguyen, T. T.; Swift, J. L.; Burger, M. C.; Cramb, D. T. *J. Phys. Chem. B* **2009**, *113*, 10357–10366.
- (7) Tcherniak, A.; Prakash, A.; Mayo, J. T.; Colvin, V. L.; Link, S. *J. Phys. Chem. C* **2009**, *113*, 844–848.
- (8) Rocker, C.; Potzl, M.; Zhang, F.; Parak, W. J.; Nienhaus, G. U. *Nat. Nanotech.* **2009**, *4*, 577–580.
- (9) Pinaud, F.; King, D.; Moore, H. P.; Weiss, S. *J. Am. Chem. Soc.* **2004**, *126*, 6115–6123.
- (10) Clancy, A. A.; Gregoriou, Y.; Yaehne, K.; Cramb, D. T. *Chem. Phys. Lett.* **2010**, *488*, 99–111.
- (11) Eck, W.; Craig, G.; Sigdel, A.; Ritter, G.; Old, L. J.; Tang, L.; Brennan, M. F.; Allen, P. J.; Mason, M. D. *ACS Nano* **2008**, *2*, 2263–2272.
- (12) Kuyper, C. L.; Budzinski, K. L.; Lorenz, R. M.; Chiu, D. T. *J. Am. Chem. Soc.* **2006**, *128*, 730–731.
- (13) Sabanayagam, C. R.; Lakowicz, J. R. *Nanotechnology* **2007**, *18*, 355402/1–355402/7.
- (14) Wang, K. L.; Qiu, X.; Dong, C. Q.; Ren, J. C. *ChemBioChem* **2007**, *8*, 1126–1129.
- (15) Octeau, V.; Cognet, L.; Duchesne, L.; Lasne, D.; Schaeffer, N.; Fernig, D. G.; Lounis, B. *ACS Nano* **2009**, *3*, 345–350.
- (16) Paulo, P. M. R.; Gaiduk, A.; Kulzer, F.; Krens, S. F. G.; Spaink, H. P.; Schmidt, T.; Orrit, M. *J. Phys. Chem. C* **2009**, *113*, 11451–11457.
- (17) Bouhelier, A.; Bachelot, R.; Lerondel, G.; Kostcheev, S.; Royer, P.; Wiederrecht, G. P. *Phys. Rev. Lett.* **2005**, *95*, 267405/1–267405/4.
- (18) Durr, N. J.; Larson, T.; Smith, D. K.; Korgel, B. A.; Sokolov, K.; Ben-Yakar, A. *Nano Lett.* **2007**, *7*, 941–945.
- (19) Farrer, R. A.; Butterfield, F. L.; Chen, V. W.; Fourkas, J. T. *Nano Lett.* **2005**, *5*, 1139–1142.
- (20) Imura, K.; Nagahara, T.; Okamoto, H. *J. Phys. Chem. B* **2005**, *109*, 13214–13220.
- (21) Loumagine, M.; Richard, A.; Laverdant, J.; Nutarelli, D.; Debarre, A. *Nano Lett.* **2010**, *10*, 2817–2824.
- (22) Wang, H. F.; Huff, T. B.; Zweifel, D. A.; He, W.; Low, P. S.; Wei, A.; Cheng, J. X. *Proc. Natl. Acad. Sci. U.S.A.* **2005**, *102*, 15752–15756.
- (23) Tirado, M. M.; Martinez, C. L.; de la Torre, J. G. *J. Chem. Phys.* **1984**, *81*, 2047–2052.
- (24) Tsay, J. M.; Doose, S.; Weiss, S. *J. Am. Chem. Soc.* **2006**, *128*, 1639–1647.
- (25) Sönnichsen, C.; Franzl, T.; Wilk, T.; von Plessen, G.; Feldmann, J.; Wilson, O.; Mulvaney, P. *Phys. Rev. Lett.* **2002**, *88*, 077402/1–077402/4.
- (26) Slaughter, L. S.; Wu, Y.; Willingham, B. A.; Nordlander, P.; Link, S. *ACS Nano* **2010**, *4*, 4657–4666.
- (27) Muskens, O. L.; Bachelier, G.; Del Fatti, N.; Vallee, F.; Brioude, A.; Jiang, X. C.; Pileni, M. P. *J. Phys. Chem. C* **2008**, *112*, 8917–8921.
- (28) Chang, W. S.; Ha, J. W.; Slaughter, L. S.; Link, S. *Proc. Natl. Acad. Sci. U.S.A.* **2010**, *107*, 2781–2786.
- (29) Al-Qadi, B.; Saiki, T. *Jpn. J. Appl. Phys.* **2010**, *49*, 125001/1–125001/6.
- (30) Gu, Y.; Sun, W.; Wang, G.; Fang, N. *J. Am. Chem. Soc.* **2011**, *133*, 5720–5723.
- (31) Pierrat, S.; Hartinger, E.; Faiss, S.; Janshoff, A.; Sönnichsen, C. *J. Phys. Chem. C* **2009**, *113*, 11179–11183.
- (32) Sönnichsen, C.; Alivisatos, A. P. *Nano Lett.* **2005**, *5*, 301–304.
- (33) Spetzler, D.; York, J.; Daniel, D.; Fromme, R.; Lowry, D.; Frasch, W. *Biochemistry* **2006**, *45*, 3117–3124.
- (34) Wang, G. F.; Sun, W.; Luo, Y.; Fang, N. *J. Am. Chem. Soc.* **2010**, *132*, 16417–16422.
- (35) Bingham, J. M.; Willets, K. A.; Shah, N. C.; Andrews, D. Q.; Van Duyne, R. P. *J. Phys. Chem. C* **2009**, *113*, 16839–16842.
- (36) Lasne, D.; Blab, G. A.; Berciaud, S.; Heine, M.; Groc, L.; Choquet, D.; Cognet, L.; Lounis, B. *Biophys. J.* **2006**, *91*, 4598–4604.
- (37) Louit, G.; Asahi, T.; Tanaka, G.; Uwada, T.; Masuhara, H. *J. Phys. Chem. C* **2009**, *113*, 11766–11772.
- (38) Xu, C. S.; Cang, H.; Montiel, D.; Yang, H. *J. Phys. Chem. C* **2007**, *111*, 32–35.
- (39) Magde, D.; Elson, E. L.; Webb, W. W. *Biopolymers* **1974**, *13*, 29–61.
- (40) Aragon, S. R.; Pecora, R. *J. Chem. Phys.* **1976**, *64*, 1791–1803.
- (41) Schwille, P.; Haupt, U.; Maiti, S.; Webb, W. W. *Biophys. J.* **1999**, *77*, 2251–2265.
- (42) Haustein, E.; Schwille, P. *Methods* **2003**, *29*, 153–166.
- (43) Kim, S. A.; Heinze, K. G.; Schwille, P. *Nat. Methods* **2007**, *4*, 963–973.
- (44) Kreibig, U.; Vollmer, M. *Optical Properties of Metal Clusters*; Springer: Berlin, 1995.
- (45) Tcherniak, A.; Ha, J. W.; Dominguez-Medina, S.; Slaughter, L. S.; Link, S. *Nano Lett.* **2010**, *10*, 1398–1404.
- (46) Gaiduk, A.; Yorulmaz, M.; Orrit, M. *ChemPhysChem* **2011**, *12*, 1536–1541.
- (47) Dulkeith, E.; Niedereichholz, T.; Klar, T. A.; Feldmann, J.; von Plessen, G.; Gittins, D. I.; Mayya, K. S.; Caruso, F. *Phys. Rev. B* **2004**, *70*, 205424/1–205424/4.
- (48) Mohamed, M. B.; Volkov, V.; Link, S.; El-Sayed, M. A. *Chem. Phys. Lett.* **2000**, *317*, 517–523.
- (49) Beversluis, M. R.; Bouhelier, A.; Novotny, L. *Phys. Rev. B* **2003**, *68*, 115433/1–115433/10.
- (50) Chen, J. J.; Irudayraj, J. *ACS Nano* **2009**, *3*, 4071–4079.
- (51) He, H.; Xie, C.; Ren, J. *Anal. Chem.* **2008**, *80*, 5951–5957.
- (52) Wu, X.; Ming, T.; Wang, X.; Wang, P.; Wang, J.; Chen, J. *ACS Nano* **2009**, *4*, 113–120.
- (53) Varnavski, O. P.; Mohamed, M. B.; El-Sayed, M. A.; Goodson, T. *J. Phys. Chem. B* **2003**, *107*, 3101–3104.
- (54) Varnavski, O. P.; Goodson, T.; Mohamed, M. B.; El-Sayed, M. A. *Phys. Rev. B* **2005**, *72*, 235405/1–235405/9.
- (55) Gaiduk, A.; Ruijgrok, P. V.; Yorulmaz, M.; Orrit, M. *Phys. Chem. Chem. Phys.* **2011**, *13*, 149–153.
- (56) Tcherniak, A.; Reznik, C.; Link, S.; Landes, C. F. *Anal. Chem.* **2009**, *81*, 746–754.
- (57) Daniels, C. R.; Reznik, C.; Landes, C. F. *Langmuir* **2010**, *26*, 4807–4812.
- (58) Kask, P.; Piksarv, P.; Pooga, M.; Mets, U.; Lippmaa, E. *Biophys. J.* **1989**, *55*, 213–220.
- (59) Wei, C.-Y. J.; Kim, Y. H.; Darst, R. K.; Rossky, P. J.; Vandenberg, D. A. *Phys. Rev. Lett.* **2005**, *95*, 173001/1–173001/4.
- (60) Hess, S. T.; Webb, W. W. *Biophys. J.* **2002**, *83*, 2300–2317.
- (61) Chang, W.-S.; Slaughter, L. S.; Khanal, B. P.; Manna, P.; Zubarev, E. R.; Link, S. *Nano Lett.* **2009**, *9*, 1152–1157.
- (62) Slaughter, L. S.; Chang, W.-S.; Swanglap, P.; Tcherniak, A.; Khanal, B. P.; Zubarev, E. R.; Link, S. *J. Phys. Chem. C* **2010**, *114*, 4934–4938.
- (63) Link, S.; El-Sayed, M. A. *J. Phys. Chem. B* **1999**, *103*, 8410–8426.
- (64) Wilcoxon, J. P.; Martin, J. E.; Parsapour, F.; Wiedenman, B.; Kelley, D. F. *J. Chem. Phys.* **1998**, *108*, 9137–9143.
- (65) Cang, H.; Montiel, D.; Xu, C. S.; Yang, H. *J. Chem. Phys.* **2008**, *129*, 044503/1–044503/5.
- (66) Al-Qadi, B. M.; Saiki, T. *J. Nanophoton.* **2009**, *3*, 039503/1–039503/6.
- (67) Knight, M. W.; Sobhani, H.; Nordlander, P.; Halas, N. J. *Science* **2011**, *332*, 702–704.
- (68) Reznik, C.; Estillore, N.; Advincula, R. C.; Landes, C. F. *J. Phys. Chem. B* **2009**, *113*, 14611–14618.
- (69) Abate, Y.; Schwartzberg, A.; Strasser, D.; Leone, S. R. *Chem. Phys. Lett.* **2009**, *474*, 146–152.
- (70) Kim, D.-S.; Heo, J.; Ahn, S.-H.; Han, S. W.; Yun, W. S.; Kim, Z. H. *Nano Lett.* **2009**, *9*, 3619–3625.
- (71) Anderson, L. J. E.; Mayer, K. M.; Fraleigh, R. D.; Yang, Y.; Lee, S.; Hafner, J. H. *J. Phys. Chem. C* **2010**, *114*, 11127–11132.